Experiments in Fluids (2026) 67:23
https://doi.org/10.1007/s00348-026-04176-4

RESEARCH ARTICLE

Photogrammetry Measurements of Blunt Body Dynamics in a Supersonic Wind Tunnel

Pietro Innocenzi[1] · Paul J. K. Bruce[2] · Salvador Navarro-Martinez[1,3]

Received: 12 September 2025 / Revised: 9 January 2026 / Accepted: 12 January 2026

Abstract

This paper presents free-oscillation experiments of a blunt body conducted in a high-speed wind tunnel, with the model motion measured using photogrammetry. A faceted blunt model, mounted on a spherical air bearing, is free to rotate in roll, pitch, and yaw in response to the freestream flow ($M = 2$). Four synchronised high-speed cameras capture the model from multiple angles, and the unique coded targets printed on the model's surface are reconstructed as points in 3D space, achieving accuracy within 1° for both static and dynamic measurements. The Kabsch algorithm is used to find the optimal rotation between two point clouds, hence allowing reconstruction of the angular motion over the entire run. The method shows promise for free-oscillation tests in high-speed ground facilities, offering advantages over ballistic range and free-flight tests such as a constant freestream velocity and hundreds of oscillation cycles. This capability enables the observation of dynamic instabilities that develop over extended timescales, thus revealing a precessional instability previously reported only for slender bodies at hypersonic Mach numbers.

1 Introduction

As an entry vehicle descends through the atmosphere, aerodynamic loads can induce spontaneous roll rates and self-exciting oscillations in pitch and yaw. Such dynamic instabilities may increase drag, alter the trajectory, impose excessive loads on the payload, and, in severe cases, cause critical failures such as malfunction of the parachute deployment system. While computational methods have come a long way in predicting aerodynamic loads and their influence on vehicle dynamics, experimental characterisation of these behaviours remains an essential step in the design of any space mission involving a novel geometry.

The demand for high-payload planetary missions has driven the development of mechanically deployable aeroshells, such as NASA's ADEPT (Cassell et al. 2017), the Italian Space Agency's IRENE (Bassano et al. 2011), and the Hypersonic Foldable Aeroshell for Thermal Protection using Origami (HATHOR), developed at Imperial College London (O'Driscoll et al. 2021). HATHOR comprises rigid panels with a thermal protection system layer, connected between eight retractable ribs, enabling a deployed diameter of 2.65 m (see Fig. 1). Following initial structural (O'Driscoll et al. 2021) and thermal load (Gramola et al. 2022; Innocenzi et al. 2022) characterisations, ongoing efforts are directed towards investigating the dynamic stability of these novel configurations. Building on earlier computational work (Innocenzi et al. 2025), this paper presents an experimental approach to measure the dynamics of a model resembling HATHOR.

Mechanically deployable aeroshells are characterised by a faceted forebody and an open aftbody, which differ significantly from conventional capsule-shaped entry vehicles, thus requiring careful dynamic characterisation. Ballistic range tests and high-fidelity CFD simulations have been conducted for ADEPT (Hergert et al. 2017), providing measurements of pitch damping under different conditions. However, because range tests and CFD can capture only a few oscillation cycles, they are unable to predict dynamic instabilities that evolve gradually over many cycles. This limitation was illustrated by the ADEPT SR-1 flight test in 2018, which revealed dynamic

✉ Pietro Innocenzi
pi120@ic.ac.uk

[1] Department of Mechanical Engineering, Imperial College London, Exhibition Rd, London SW7 2AZ, UK

[2] Department of Aeronautics, Imperial College London, Exhibition Rd, London SW7 2AZ, UK

[3] Aragón Institute of Engineering Research (I3A), Fluid Mechanics Department, University of Zaragoza, Zaragoza 50018, Spain

Published online: 28 January 2026

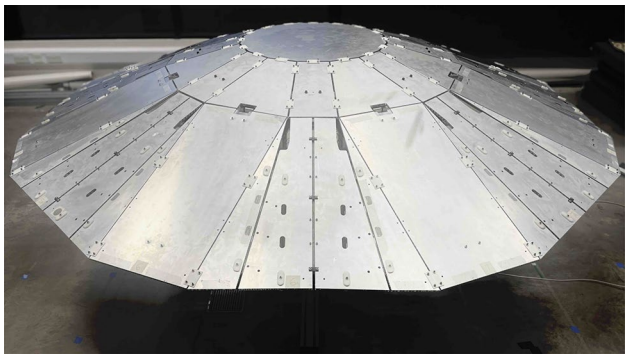

Fig. 1 Deployed 2.65 m engineering model of Imperial College London's HATHOR concept (O'Driscoll et al. 2021)

instabilities in angle of attack associated with the onset of high roll rates (Dutta et al. 2022).

An alternative to ballistic range is free-oscillation wind tunnel testing, in which the model is mounted on a pivot and permitted to rotate in one or more rotational degrees of freedom in response to the aerodynamic moments of the incoming flow. Gas bearings are generally preferred as pivots because they introduce negligible tare damping. Compared to ballistic range and free-flight testing, this technique enables the study of model dynamics at constant freestream velocity over several seconds, corresponding to hundreds of oscillation cycles. Its main limitations arise from the influence of the sting and tunnel walls, which can modify the wake flow and affect aerodynamic damping, and from the simplifying assumption of 3-DoF motion, which remains an approximation of the true 6-DoF dynamics.

Although 1-DoF free-oscillation tests are common, publicly available studies involving 3-DoF gas bearing rigs at high speed are limited to the work of Ward et al. (1972), who investigated a slender cone at hypersonic speed. The present study extends this approach by developing an experimental method for investigating blunt body dynamics in a supersonic wind tunnel, enabling large-amplitude motion ($\pm 15°$ in pitch and yaw, 360° in roll) over extended periods with high temporal resolution.

Dynamic motion can be measured with on-board sensors such as angular potentiometers, Hall effect sensors, and inertial measurement units (IMUs). However, the small test sections of some supersonic and hypersonic facilities can constrain model size and preclude the integration of on-board sensors. Moreover, on-board instrumentation alters the model's mass, stiffness, and damping, thereby affecting the true dynamics. To overcome these limitations, this paper presents a robust method based on stereo photogrammetry to capture the model's motion for extended periods of time during supersonic runs.

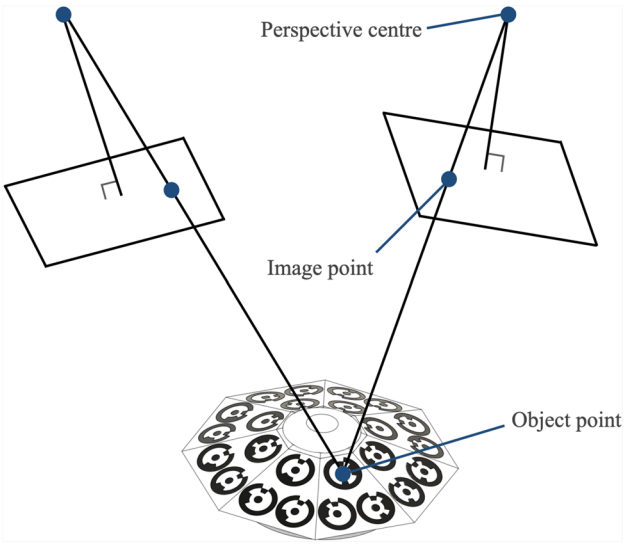

Fig. 2 Pinhole camera model for stereo photogrammetry

1.1 Photogrammetry for wind tunnel measurements

Photogrammetry is a non-invasive measurement technique used to determine the displacement of points, patterns, or features on a subject based on images captured by cameras. The specific type of photogrammetry is typically classified according to the nature of the targets being tracked. While the present work focuses on *point-tracking photogrammetry*, other approaches include *digital image correlation* (DIC), where a random speckle pattern is applied to the surface, and *targetless methods*, in which natural features of the object are tracked (Baqersad et al. 2017).

In point-tracking photogrammetry, optical targets are applied to the test article using methods such as adhesive stickers, mask painting, or integration during manufacturing to preserve the original aerodynamic surface. Their positions are determined using ellipse-detection algorithms or advanced image processing techniques. Targets may be non-coded or coded: the former require less surface area and are easier to detect, whereas the latter are uniquely identifiable and remain trackable regardless of the displacement magnitude between successive frames.

The 3D position of a target is determined by triangulating the rays that connect the object point (i.e. the physical target) to its corresponding image point (the target's projection in the 2D image) through the perspective centre (the effective optical projection point of the camera, located within the lens system). In the pinhole camera model, which provides the mathematical framework for computing target coordinates, the perspective centre is conventionally illustrated behind the image plane, see Fig. 2. When the intrinsic and

extrinsic parameters of the cameras are known from calibration, these rays can be reconstructed precisely, enabling accurate determination of the target coordinates. While two cameras are sufficient for triangulation, using at least four is generally preferred, as the redundancy reduces the overall error. Uncertainty of the measurement is usually dependent on the quality of the calibration, the number of cameras used, the camera angle, the resolution, the shutter speed, and the amplitude of the displacement and its rate.

Point tracking photogrammetry has been widely employed in wind tunnel tests due to its non-contact and full-field capabilities. Tests have been performed in subsonic, transonic, and supersonic facilities, with applications focusing on aeroelastic analysis, attitude measurement, and rigid-body dynamics. Early work by Brooks and Beamish (1977) applied photogrammetry to measure aeroelastic deformations of an aircraft model at transonic speeds, reporting reduced accuracy during dynamic motion compared to static conditions. Schairer and Hand (1999) measured aeroelastically damped and self-oscillatory clipped delta wings, finding frequency predictions within 3% of strain-gauge measurements and damping standard deviations within 6% of the mean value. Kushner et al. (2013) measured the deformations of a 6 m diameter model of the hypersonic inflatable aero-decelerator (HIAD) at subsonic speeds, with Li et al. (2014) extending the work to measure the static and dynamic response under various loading conditions. Gramola et al. (2019) used photogrammetry in the Imperial College London supersonic tunnel to quantify SBLI-induced deformations on a flexible plate, estimating the uncertainties due to optical distortion in compressible flows to be below 0.03 mm. Schairer et al. (2021) measured the elastic bending, twist, and attitude of a three-bladed rotor in forward flight, with agreements between photogrammetry and Hall effect sensors in pitch and flap angles within 1°.

Beyond aeroelastic deformation, photogrammetry has been used to measure position, attitude, and rigid-body dynamics. Watzlavick et al. (1996) compared photogrammetry to precision accelerometers and laser interferometers for angle of attack measurements of aircraft models at transonic speeds, reporting uncertainties as low as $\pm 0.01°$ across all methods, but limiting the analysis to static measurements in 1-DoF. Schairer et al. (2017) measured the position and attitude of a slender body during nozzle-plume/shock-wave interactions at supersonic speeds, also limiting the analysis to static measurements in angle of attack only. Muller et al. (2019, 2020) employed photogrammetry on a free-oscillation rig to capture low-amplitude pitch and yaw oscillations of a finned slender body from subsonic to low supersonic speeds, fitting the data to a 1-DoF equation to extrapolate the pitch damping coefficient. Their method showed promise, although it was limited to only a few oscillation cycles per test and constrained by rig characteristics such as the use of mechanical bearings and a maximum oscillation amplitude of 2°.

Photogrammetry has also been widely adopted to measure the dynamics of models in hypersonic free-flight wind tunnel tests and derive their aerodynamic coefficients. Seltner et al. (2019) employed point-tracking photogrammetry to measure the 6-DoF motion and aerodynamic coefficients of free-flying cubes at hypersonic speeds over a broad range of attitudes, reporting spatial uncertainties on the order of tens of μm. Starshak and Laurence (2021) applied an edge-fitting technique to determine the 5-DoF and 6-DoF free-flight dynamics of blunt bodies in hypersonic flow, achieving sub-μm tracking precision and determining aerodynamic coefficients with uncertainties below 4%. Hyslop et al. (2024) compared aerodynamic force coefficients obtained using a sting-mounted balance and free-flight measurements, where model motion was tracked by both an IMU and a 2D point-tracking method; the free-flight approach yielded approximately half the uncertainty of the balance, with comparable results between the IMU and the optical technique. Lock et al. (2025) developed a photogrammetric framework based on a sigma-point Kalman filter with Rauch–Tung–Striebel smoothing to reconstruct the 6-DoF motion and aerodynamic coefficients of a free-flying cube in hypersonic flow, achieving force coefficient uncertainties of 0.6–3.4% and moment coefficient uncertainties of 4.7–26.8% (with higher values corresponding to higher rotation rates).

While some of these studies successfully captured the dynamics of wind tunnel models, their utility for stability analysis was limited by the small number of oscillation cycles achievable within the employed experimental setups. The present work demonstrates that, when combined with a free-oscillation setup in a blow-down facility, photogrammetry can be used to measure the model motion over hundreds of oscillation cycles in a single test.

2 Experimental method

2.1 Imperial supersonic wind tunnel

The Imperial College supersonic wind tunnel is a blow-down facility with a $150 \times 150 \times 727$ mm test section capable of Mach numbers up to 2.7. A tunnel schematic is provided in Fig. 3. The test conditions for this study are presented in Table 1. To showcase the steadiness of the freestream flow during the runs, Fig. 4 presents the total pressure in the settling chamber and the static pressure measured at the end of the flat-side de Laval nozzle, both normalised with respect to the reference total pressure $p_{0,\mathrm{ref}} = 1.8 \cdot p_e$, where p_e is the ambient pressure. The test section Mach number is estimated from these values via the isentropic flow relation. The total temperature, computed with a thermocouple in the settling

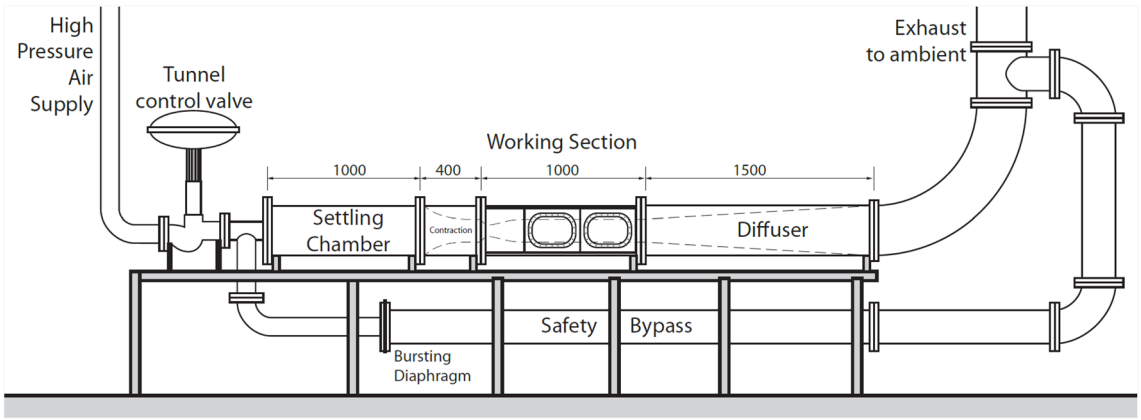

Fig. 3 Schematic of Imperial College London's supersonic wind tunnel facility

Table 1 Wind tunnel test conditions

M	p_0/p_e	T_0 [K]	q [Pa]	Re_D ($D = 40$ mm)
2.0	1.8	290	6.53×10^4	9.3×10^5

chamber, is on average $T_0 = 290$ K and decreases during a run with an average gradient of $dT_0/dt = -0.9$ K/s, which leads to a small gradient in freestream Reynolds number $dRe_\infty/dt = 0.007Re_\infty\, s^{-1}$, which is not expected to affect the present experiments. Threadgill (2017) characterised the tunnel flow with PIV and determined the presence of a non-uniform, nonzero wall-normal component in the freestream flow, $|v/U_\infty| < 1\%$ (where v is the wall-normal velocity component and U_∞ the freestream velocity magnitude), which translates into a non-uniform flow angularity $< 0.6°$.

2.2 Experimental rig

Figure 5 shows the experimental rig employed in this study. At its core is a spherical air bearing that supports a freely oscillating model. The bearing is housed within a seamless steel tube, which is fastened to the tunnel ceiling by a 12 mm solid steel block.

The air bearing is from New Way Air Bearings (part number S3625R), featuring a 25 mm casing diameter and surface radius of curvature. The concave surface is made of porous graphite, and interfaces with an aluminium spherical cap, providing a thin film of air at 8 bar separating the ball and the graphite surface. The model is extended from the spherical cap by a shaft such that the centre of rotation (CoR) of the model sits at the desired centre of gravity (CoG) position, which is 34.5% of the model diameter D aft of the nose. Figure 5b shows a detailed view of the front of the rig, with the moving components shaded green and the stationary air bearing shaded pink.

During tunnel operation the model and cap are kept in place by the drag force acting axially on the model. A moving-arm system has been implemented to hold the model captive prior to tunnel start-up. The system is actuated by a stepper motor and lead screw to open and provide up to ±15° of free oscillation in pitch and yaw and 360° in roll during tunnel runs.

Test articles are printed on a Stratasys J850 system using VeroUltra, a high-performance rigid photopolymer. The printer operates with a layer thickness down to 14 μm, dimensional deviations within ±100 μm and an average surface roughness (Ra) in the range of 0.5 – 4 μm. Although

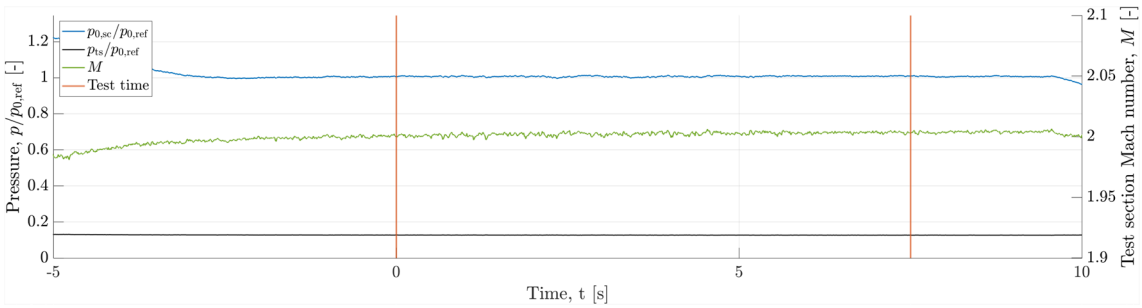

Fig. 4 Measured pressure in stagnation chamber (sc) and test section (ts) alongside estimated freestream mach number

this method provides excellent geometric fidelity for small-scale models, slightly higher mass non-uniformities are expected compared to conventional CNC machining, due to the layer-by-layer deposition process and minor inhomogeneities in material curing. The influence of small mass non-uniformities on dynamic stability is discussed in Sect. 3.2. By employing the printer's multi-channel material capability, uniquely coded targets are printed in black within the last layers of the model's forebody using the same photopolymer (while the rest of the model is printed in white), thus preserving uniform material properties and surface finish. The articles, with maximum diameter $D = 40$ mm, resemble the faceted forebody and open aftbody of mechanically deployable aeroshells. Each rib is fitted with a roll generator at its tip, breaking the flow symmetry and producing a net static roll moment. Figure 6 shows the model geometry and the rig installed in the test section.

2.3 Dynamic scaling

Table 2 presents the geometric and mass properties of the model. Moments of inertia and CoG values are estimated from the CAD geometry and computed with respect to the CoR (located 34.5%D aft of the nose).

Due to the presence of the metal cap and shaft, the moment of inertia about the pitch axis is greater than that

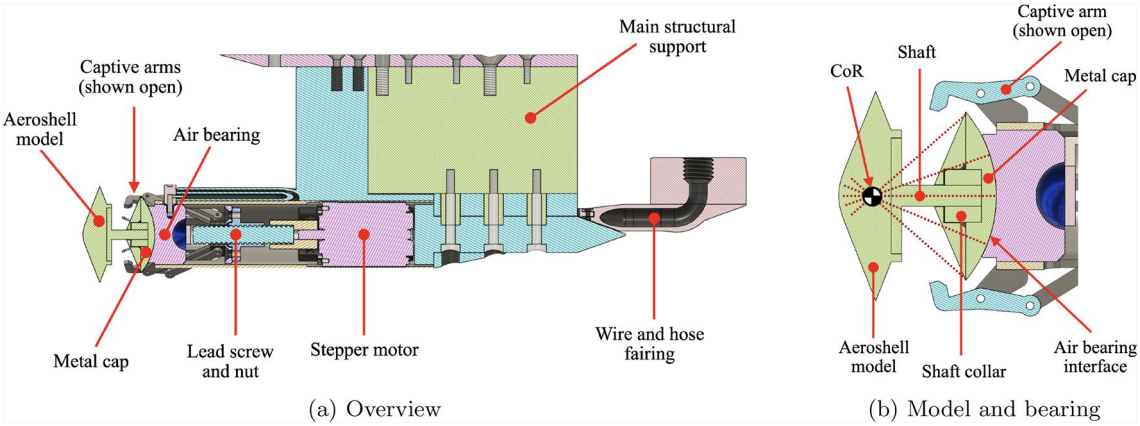

Fig. 5 Cross section of experimental rig with major components labelled

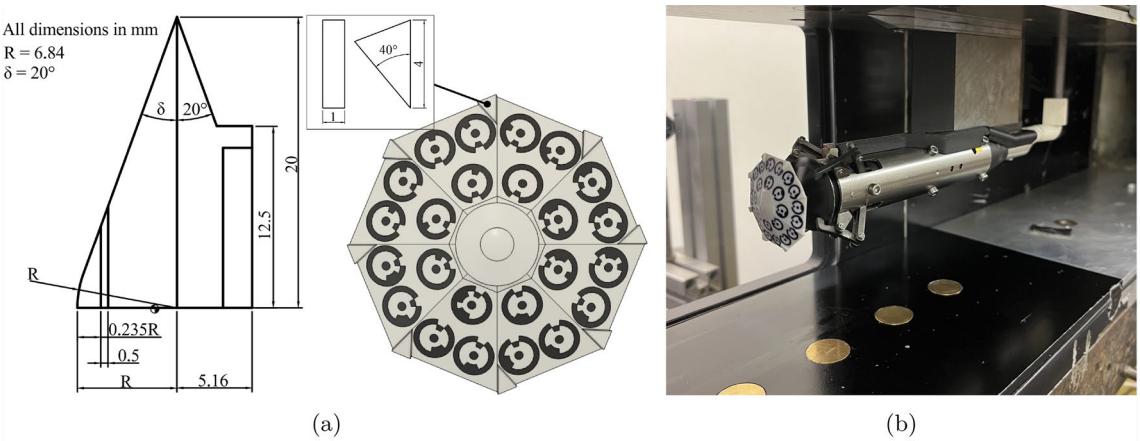

Fig. 6 **a** Model geometry: side view of the axisymmetric model (no facets) and roll generator geometry. **b** Experimental rig installed in the tunnel test section

Table 2 Model properties

D [mm]	I_{xx} [g · mm^2]	$I = I_{yy} = I_{zz}$ [g · mm^2]	I_{xx}/I [-]	CoG [mm]	St_0 [-]
40	1514	4618	0.34	[−12.2, 0, 0]	0.021

about the roll axis, resulting in a moment of inertia ratio $\mu = I_{xx}/I = 0.34$. This value contrasts with those typical of deployable aeroshells (for instance, the ADEPT SR-1 test vehicle was characterised by $\mu = 1.5$, see Judd 2023). This ratio is particularly relevant to the dynamic stability analysis of rolling entry vehicles, as Nicolaides (1953) demonstrated that roll resonance can occur only for configurations with $\mu < 1$, thus indicating that the model used in the present tests is capable of locking into resonance. Additionally, due to the metal cap, the CoG of the model sits 12.2 mm behind the CoR. This induces a pitch-up moment which is readily restored by the aerodynamic moment in pitch. Since static RANS results indicate that $mgl/M_{\text{aero}}(\theta = 10°) \simeq 3\%$, this CoG shift along the roll axis is not expected to significantly influence the dynamics. Its effect is discussed further in Sect. 3.2. The natural frequency in pitch, derived by Nicolaides (1953), is

$$St_0 = \frac{D}{U_\infty} 2\pi f = \frac{D}{U_\infty} \sqrt{\frac{\rho_\infty U_\infty^2 SD|c_{m_\theta}|}{2I_{yy}}} , \tag{1}$$

where St_0 is the non-rolling undamped Strouhal number in pitch, f is the non-rolling undamped frequency of oscillations in pitch, S is the projected frontal surface of the model, and c_{m_θ} is the pitch moment slope, estimated in this work with static RANS. During the final portion of entry, the value of St_0 varies based on the trajectory, atmospheric properties, and vehicle geometry, with typical values of $\mathcal{O}(0.01)$-$\mathcal{O}(0.1)$ (Owens and Aubuchon 2011; Owens et al. 2024). The reduced frequency of the present study ($St_0 = 0.021$) therefore scales well with actual entry trajectories. Understanding how the dynamics scale at lower or higher frequencies is also of particular interest, but investigations into the effect of Strouhal number on dynamic stability are limited. Whitlock and Siemers (1972) performed 1-DoF free-oscillation tests for the Viking-type entry vehicle at $M = 1.76$ and three values of Strouhal number $St_0 = [0.0138, 0.038, 0.058]$, indicating a nonlinear increase in dynamic stability at lower frequency of oscillations. Owens and Aubuchon (2011) performed 1-DoF forced oscillation of the Orion Crew Module at $M = 0.3$ and $St_0 = [0.136, 0.274, 0.492]$ indicating the opposite trend. Owens et al. (2024) run 1-DoF forced oscillation tests of the Dragonfly aeroshell at a range of Mach numbers from 0.04 to 1.05 and Strouhal numbers from 0.026 to 0.8, confirming increased instabilities at lower frequency of oscillations. Innocenzi et al. (2025) performed 1-DoF free-oscillation Detached Eddy Simulations of a deployable geometry at $M = 2$ and $St_0 = [0.02, 0.06, 0.12]$, also suggesting increased instabilities at lower Strouhal numbers. While most of the recent studies seem to suggest higher instabilities at lower reduced frequencies, the trends are highly nonlinear and sometimes contradicting, making the current tests hard to scale to different values of Strouhal number. Ongoing work aims to use the current setup to study reduced frequency effects, by testing models with unchanged geometry and different moments of inertia.

2.4 Photogrammetric setup

Four synchronised cameras are arranged to view the model from maximally separated angles, minimising triangulation error. While the theoretical optimum separation is 90° in both vertical and horizontal planes, the rig location with respect to the tunnel windows constrained the setup to around 80° and 45° in the vertical and horizontal planes, respectively. The camera and lens models are presented in Table 3.

The four cameras are synchronised through an F-Sync connection, which links their internal clocks via BNC cables to ensure frame-level timing alignment. All cameras communicate with the control computer over Ethernet, and image acquisition is triggered by a National Instruments DAQ controlled through a LabVIEW VI, which initiates recording simultaneously with the opening of the mechanical arms.

The commercial photogrammetry software PhotoModeler Premium 2022.2.0 (PhotoModeler Technologies 2022) is used to calibrate the cameras and obtain their intrinsic parameters. These include the focal length, principal point, and lens correction factors (radial distortions K_1 and K_2, decentring distortions P_1 and P_2). The intrinsic camera calibration is performed off-site, taking photographs from different locations and orientations of a calibration grid characterised by a target pattern. To achieve a highly accurate calibration, guidelines are followed: (1) the target pattern is kept flat and clean, (2) the target pattern fills most of the camera view finder, (3) the camera orientations are kept at 45° from the horizontal and vertical planes, respectively, (4) all snapshots are taken with the same focus settings, (5)

Table 3 Camera and lens configurations used in the study

	Cam. 1	Cam. 2	Cam. 3	Cam. 4
Camera model	Phantom VEO640	Phantom VEO640	Phantom V641	Phantom M310
Sampling rate	1.5 kHz			
Exposure time	150 μs			
Lens focal length	60 mm	60 mm	50 mm	105 mm
Lens aperture	f/11			

cameras are placed at the same distance of the wind tunnel test. This enabled to achieve a highly accurate calibration (PhotoModeler Technologies recommends a total calibration error below 0.4 for high-accuracy projects, and this criterion was satisfied for all cameras). The extrinsic parameters (camera positions and orientations relative to the test article) are determined automatically in PhotoModeler through a bundle adjustment process.

While the high-speed cameras used in this study can achieve sampling rates up to 290 kHz, the sampling rate is set to 1.5 kHz to record the motion during the whole run (which lasts around 4.5 s). The exposure time is set to 150 μs to obtain sharp snapshots at the maximum rates experienced by the model, which are about 40 Hz. Lens aperture is set to f/11 to increase depth of field. Two LED lamps with 11000 lx are placed on either side of the test section to cope with the short exposure time and small aperture. The camera setup is shown in Fig. 7.

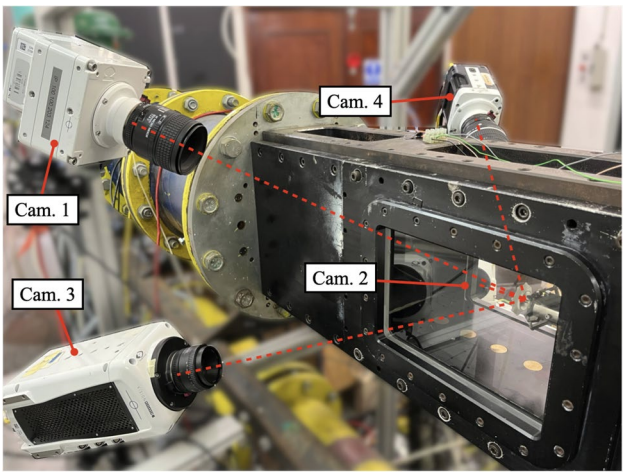

Fig. 7 Setup of four high-speed cameras in wind tunnel facility

2.5 Data processing

2.5.1 From 2D images to points in 3D space

During the wind tunnel run, synchronised images are recorded by the four high-speed cameras at each of the N sampling instants (or epochs). The $N \times 4$ images are processed with the commercial software PhotoModeler Premium 2022.2.0 to obtain a 3D point cloud at each epoch, where every 3D point corresponds to a coded target. Processing the photographs in PhotoModeler involves associating the photographs to the respective calibrated cameras, reconstructing the point cloud at the first epoch, and tracking the coded targets for the remaining $N - 1$ epochs. The tracking can be automated allowing to process high numbers of photographs per run (around 7000×4 per test in this work). A sample instant is shown in Fig. 8 with the associated reconstructed 3D point cloud.

2.5.2 From points in 3D space to orientation history

The point cloud history is imported into MATLAB, and a Kabsch algorithm is used to compute the body-angle history. The algorithm computes the body-angle increment between the current epoch and the reference epoch at $t = 0$ s (when the model is aligned with the freestream) by minimising the root-mean-square deviation of the optimal rotation and translation between the two sets of paired points. That is, given two sets of corresponding points

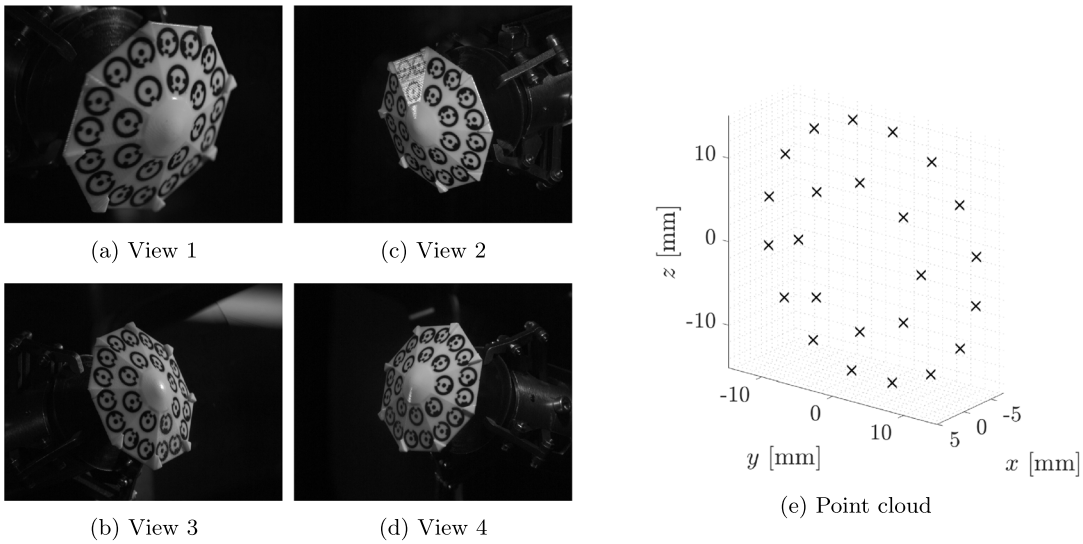

Fig. 8 Camera views and associated 3D point cloud at a single instant

$$\mathcal{P} = \{\boldsymbol{p}_1, \boldsymbol{p}_2, \ldots, \boldsymbol{p}_n\}, \quad \mathcal{Q} = \{\boldsymbol{q}_1, \boldsymbol{q}_2, \ldots, \boldsymbol{q}_n\},$$

where n is the number of points in the point cloud, the algorithm finds the rotation matrix R and the translation vector $\boldsymbol{t}$ such that

$$(R, \boldsymbol{t}) = \underset{R \in \mathrm{SO}(3),\ \boldsymbol{t} \in \mathbb{R}^3}{\operatorname{argmin}} \sum_{i=1}^{n} \left\| R\boldsymbol{p}_i + \boldsymbol{t} - \boldsymbol{q}_i \right\|^2. \tag{2}$$

The Kabsch algorithm is presented in Fig. 9. For a detailed derivation, see Sorkine-Hornung and Rabinovich (2017). In this work, the model is constrained in the translation DoFs by the spherical bearing. For all tests, the value of optimal translation remains well below 0.5 mm but is nonzero. This is likely due to: (1) the finite stiffness of gas bearings (which allow for minimal translations), (2) vibration of the frame supporting the cameras, (3) errors due to optical distortions, either from density gradients in compressible flows or from wind tunnel windows, (4) triangulation errors.

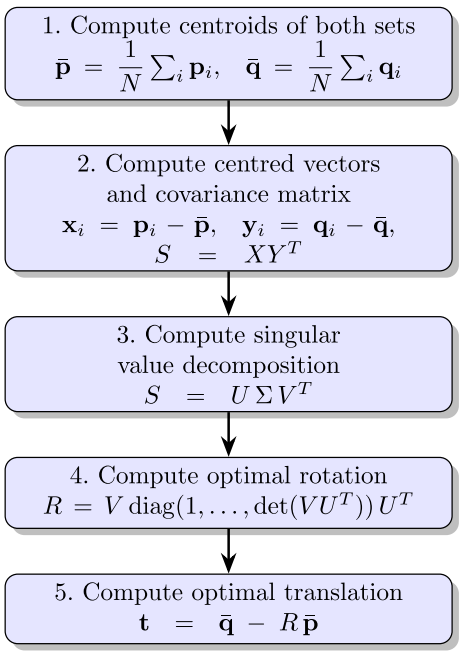

Fig. 9 Block diagram of the Kabsch algorithm

3 Results and discussion

3.1 Measurement characteristics

3.1.1 Static accuracy

Figure 10 compares the measured target positions with the CAD-predicted locations. Measurements were acquired under steady supersonic flow in the test section, prior to model release. The mean error is [0.024, 0.009, 0.007] mm and the RMSE is [0.057, 0.039, 0.227] mm along the x (roll), y (pitch), and z (yaw) axes, respectively. The x- and y-axis RMSE values are of the same order as the optical distortion uncertainty reported by Gramola et al. (2022) for compressible flows (< 0.03 mm) and within the 3D printer dimensional deviations $\pm 100\ \mu$m. The larger z-axis RMSE (evident in Fig. 10) reflects the reduced camera intersection angle along that axis ($\simeq 45°$ due to the limited size of the windows) and potential optical distortion caused by the windows.

Using Rodrigues rotation formula $R(\theta) = I + \sin\theta\,[\mathbf{u}]_\times + (1 - \cos\theta)\,[\mathbf{u}]_\times^2$, where θ is the rotation angle (e.g. pitch), $\mathbf{u}$ the corresponding unit axis (e.g. y), and $[\mathbf{u}]_\times$ the skew-symmetric cross-product matrix (see Hartley et al. (2013)), the small-angle linearisation $R(\delta\theta) \approx I + \delta\theta[\mathbf{u}]_\times$ gives the first-order displacement $\Delta\mathbf{r} = (R - I)\mathbf{r} \approx \delta\theta(\mathbf{u} \times \mathbf{r})$. Let $\mathbf{E}_i$ be the per-target residual and $\mathbf{r}_i$ the lever arm from the rotation centre. The per-point angular error about axis $\mathbf{u}$ is then

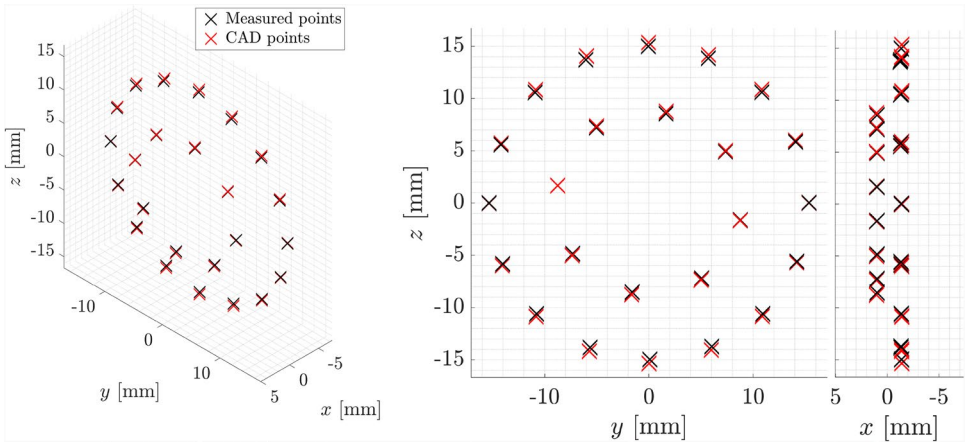

Fig. 10 Target positions: measured by photogrammetry (black) and predicted by CAD model (red). From the left: isometric, front, and side views

$$\delta\theta_i \approx \frac{\mathbf{E}_i \cdot (\mathbf{u} \times \mathbf{r}_i)}{\|\mathbf{u} \times \mathbf{r}_i\|^2}.$$

The mean per-point angular error is [0.09°, 0.06°, 0.02°], and the per-point RMSE is [0.51°, 0.33°, 0.74°] along the x (roll), y (pitch), and z (yaw) axes.

3.1.2 Uncertainty and resolution

Propagated uncertainty

An estimate of uncertainty based on error propagation is proposed in the following section. Given that $\Delta\mathbf{r}_i \approx \delta\boldsymbol{\theta} \times \mathbf{r}_i = -[\mathbf{r}_i]_\times \delta\boldsymbol{\theta}$, the covariance of the small rotation $\delta\boldsymbol{\theta}$ is given by (see Hartley and Zisserman (2004), Sec. 5.2)

$$\mathrm{Cov}(\delta\boldsymbol{\theta}) = \left(\sum_{i=1}^{N} J_i^\top \boldsymbol{\Sigma}^{-1} J_i \right)^{-1} = \left(\sum_{i=1}^{N} [\mathbf{r}_i]_\times^\top \boldsymbol{\Sigma}^{-1} [\mathbf{r}_i]_\times \right)^{-1}, \tag{3}$$

where $J_i = -[\mathbf{r}_i]_\times$ is the Jacobian of the displacement with respect to the rotation and $\boldsymbol{\Sigma} = \mathrm{diag}(\sigma_x^2, \sigma_y^2, \sigma_z^2)$ is the anisotropic covariance matrix of the measured data, with σ_x^2, σ_y^2, and σ_z^2 approximated by the per-point RMSE. The resulting 1σ orientation uncertainty is [0.045°, 0.063°, 0.062°] about the x (roll), y (pitch), and z (yaw) axes, respectively. The 95% detection threshold is defined as $1.96\,\sigma_\theta$, yielding [0.089°, 0.123°, 0.121°] about the same axes, which define the angular resolution of the method. These values represent a theoretical prediction based on the assumed measurement noise characteristics, rather than an empirical dispersion from repeated measurements. The underlying assumptions are Gaussian, zero-mean, uncorrelated measurement noise, small-angle linearisation, an exact CAD geometry, and a single static epoch considered representative of the experimental configuration. Potential systematic biases (due to calibration, refraction, or the reduced camera intersection angle along the z-axis) have not been explicitly corrected and may increase or decrease the estimated uncertainties.

Empirical uncertainty

Empirical uncertainty is obtained by performing a supersonic *static* test, in which the model is locked and the roll, pitch, and yaw angles remain zero. Test results are shown in Fig. 11. The resulting 1σ orientation uncertainty is [0.006°, 0.005°, 0.007°] about the x (roll), y (pitch), and z (yaw) axes, which is comparable to the values reported by Watzlavick et al. (1996). The 95% detection threshold yields [0.011°, 0.010°, 0.014°] about the same axes. These values take into account changes in the refraction index due to the tunnel windows and the compressible flow, as well as vibrations of the frame on which the cameras are mounted, because both were present during image acquisition. A source of error that can affect the estimate is the presence of high rotation rates. While the exposure time ensures that all snapshots are sharp, larger errors are expected when the model rotates rapidly, and this effect is not accounted for in the present analysis. Note that the current estimate is approximately an order of magnitude lower than the propagated estimate, likely because Eq. 3 uses per-point RMSE values, while the Kabsch algorithm averages these errors over all targets when estimating the pose.

3.2 Application to blunt body dynamic stability

3.2.1 Sting and wall effects

The model shown in Fig. 6a is tested at $M = 2$ and $Re_D = 9.3 \times 10^5$. Shadowgraph and Schlieren snapshots of the flowfield are presented in Fig. 12. The Shadowgraph, focused upstream of the test section to increase sensitivity, was captured with an exposure time of 1 μs, revealing the instantaneous structure of the shear layers. The Schlieren, focused at the centre of the test section to minimise Shadowgraph effects, was captured with an exposure time of 150 μs, providing a representation of the time-averaged shear-layer geometry. Additional illumination was provided from the camera side to enhance model visibility, resulting in a front-light Schlieren configuration. The images highlight the main flow features: the

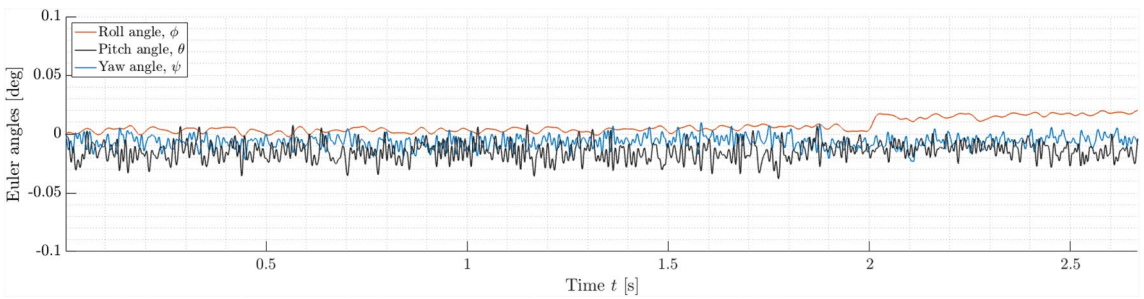

Fig. 11 Euler angles for a static test, measured with photogrammetry

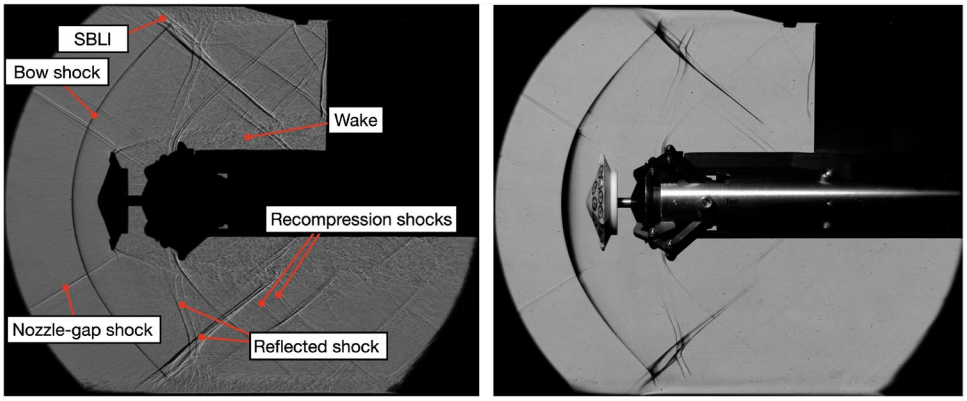

(a) Shadowgraph (b) Front-light Schlieren

Fig. 12 Flowfield for the free-oscillation rig at $M = 2$ (arms closed)

bow shock ahead of the model, the separated recirculating region downstream, and the weak, unsteady recompression shocks associated with the wake geometry. Shock-Wave Boundary Layer Interactions (SBLI), caused by the bow shock interacting with the tunnel wall boundary layers, are also present. A pair of incident shocks, labelled in the figure as *nozzle-gap shocks*, are observed as well. These shocks originate from the small gap between the nozzle and the test section walls and are very weak, as the measured rise in static pressure across them is approximately 2%. When the model pitches to high angles, the pressure at one shoulder may become slightly higher than that corresponding to a clean freestream without incident shocks. If this small pressure increase were to influence the system dynamics, it would likely lead to a marginal reduction in static stability and a slight increase in dynamic stability.

To assess the effect of the sting and wind tunnel walls, Detached Eddy Simulations (DES) of the geometry are performed in STAR-CCM+ at the same conditions of the wind tunnel tests. Three additional geometries are tested: a case with no sting and no walls, a case with walls and no sting, and a last case with walls and a reduced sting frontal area (with a sting frontal area only 33% of the nominal value). Mach number contours are shown in Fig. 13. Details of the numerics, models, and mesh are presented in Innocenzi et al. (2025).

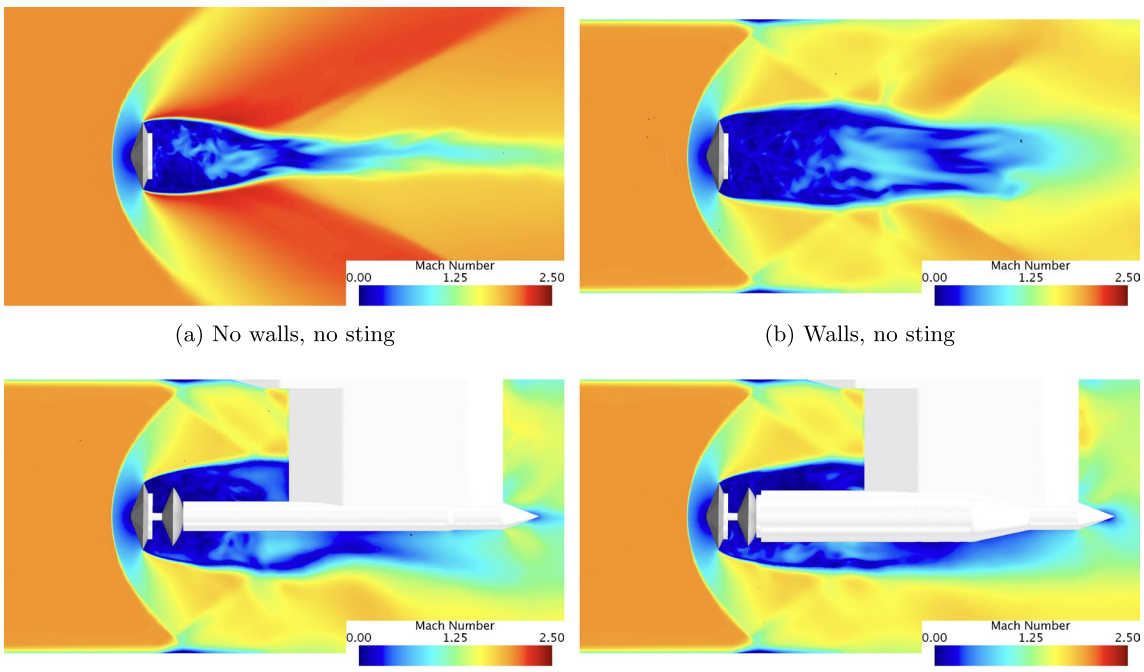

(a) No walls, no sting (b) Walls, no sting

(c) Walls, small sting (d) Experimental conditions

Fig. 13 Snapshot contours of local mach number at $M = 2$, obtained with CFD

The wake in Fig. 13a presents qualitatively the same geometry found in experimental and numerical visualisations of entry vehicle ballistic range tests (see, e.g. Hergert et al. (2017)), with a separated recirculating region remarkably smaller than in the wind tunnel tests performed in this study. The change in wake geometry seems not to be caused by the presence and size of the axial sting (see the similar wake geometries in Figs. 13b, c and d), but rather by the presence of wind tunnel walls. It is found that the thickness of the boundary layer after the SBLI can greatly influence the RANS solution used to initialise the DES. If the boundary layer thickness after the SBLI is smaller than in the contours of Fig. 13 (e.g. due to lower inlet-model distance or more dissipative mesh at the walls), the RANS predicts a smaller wake analogous to the case with no walls. This suggests that the outer shape of the wake depends more on the sectional area available to the inviscid flow rather than bodies present in the wake itself.

Unsteady aftbody pressure loads, induced by one or multiple flow modes in the wake, are often responsible for the diverging pitch oscillations observed in blunt bodies at low supersonic speeds. The influence of axial stings on the dynamics has long been a subject of debate, with no consistent trends identified (see, e.g. Schueler et al. (1967); Kazemba et al. (2017) for relevant discussions). In the present setup, the combined effects of the walls and the sting within the wake are expected to alter the damping in pitch relative to that of a ballistic range configuration, although the qualitative and quantitative nature of this influence remains uncertain.

Figure 14 shows the Euler angles history from the moment the model without roll generators is released, after steady supersonic flow is achieved in the test section. The maximum pitch and yaw angles are restricted during the first 3 s of the run, because of the gradual opening of the mechanical arms, see the black linear lines in the plot. The figure reveals how, for the case with no roll moments, the model sits at a small, nonzero trim in pitch ($\theta \simeq 2°$), likely due to the shifted CoG along the roll axis as well as the non-symmetric wake caused by the presence of the strut. A small nonzero yaw trim is also present ($\psi \simeq 0.5°$), possibly due to manufacturing imperfections and a non-uniform freestream flow. The model undergoes limit cycle oscillations in pitch and yaw of maximum amplitude $\pm 0.5°$ and frequency $St_d = 0.022$, which is 5% higher than the predicted undamped value, likely due to the inertia values obtained via CAD and the moment slope computed via RANS to be slightly off, as well as the presence of a nonzero roll rate. The model exhibits very small roll rates, likely due to unsteady wake loads as well as an asymmetric flow in the air bearing gap. Overall, the dynamics are very stable for this configuration. Dynamic instabilities observed for the model with roll generators are thus unlikely to be driven by flow modes in the recirculation region, but rather by other mechanisms, as discussed in the following sections.

3.2.2 Motion history with roll generators

Figure 15a shows the Euler angles history from the moment the model with roll generators is released, after steady supersonic flow is achieved in the test section. Between $t = 1$ s and $t = 1.35$ s, the model's cap repeatedly impacted the mechanical arms at positive pitch angles. The predicted maximum pitch angle permitted by the arms agrees closely with the measured maximum amplitude during these events, with deviations of only $\simeq 0.6°$, providing an indication of the dynamic accuracy of the photogrammetry method.

From $t = 1.7$ s to $t = 3.2$ s, the model settles into limit cycle oscillations in pitch and yaw, with amplitude between $-5.5°$ and $+7°$. After a brief transition, from $t = 3.4$ s until the end of the measurement, it oscillates between $-7.5°$ and $+10°$. The asymmetric nature of the limit cycle hints that the model has a nonzero aerodynamic trim, and that the magnitude of the trim increases with the roll rate. It is also evident that the pitch and yaw frequencies increase with roll rate, as expected from the coupling of nutation and precession with roll rate.

The Euler angles are smoothed using a zero-phase, fourth-order Butterworth low-pass filter prior to differentiation to obtain the angular rates. Distinct cut-off

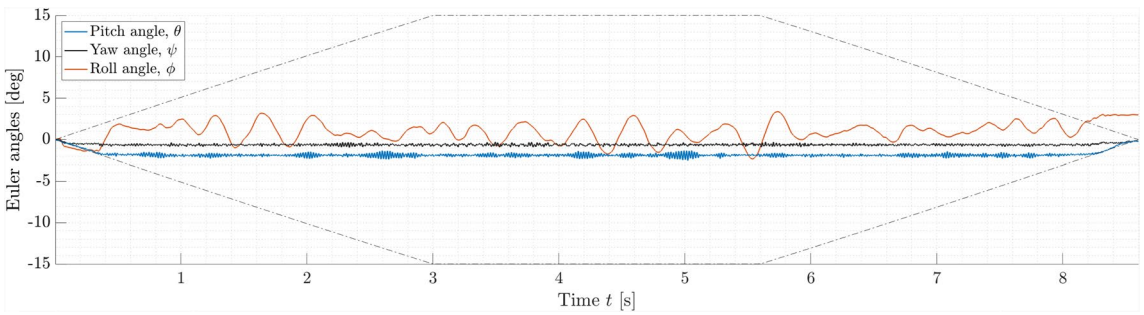

Fig. 14 Euler angles for the faceted aeroshell model with no roll generators at $M = 2$, measured with photogrammetry

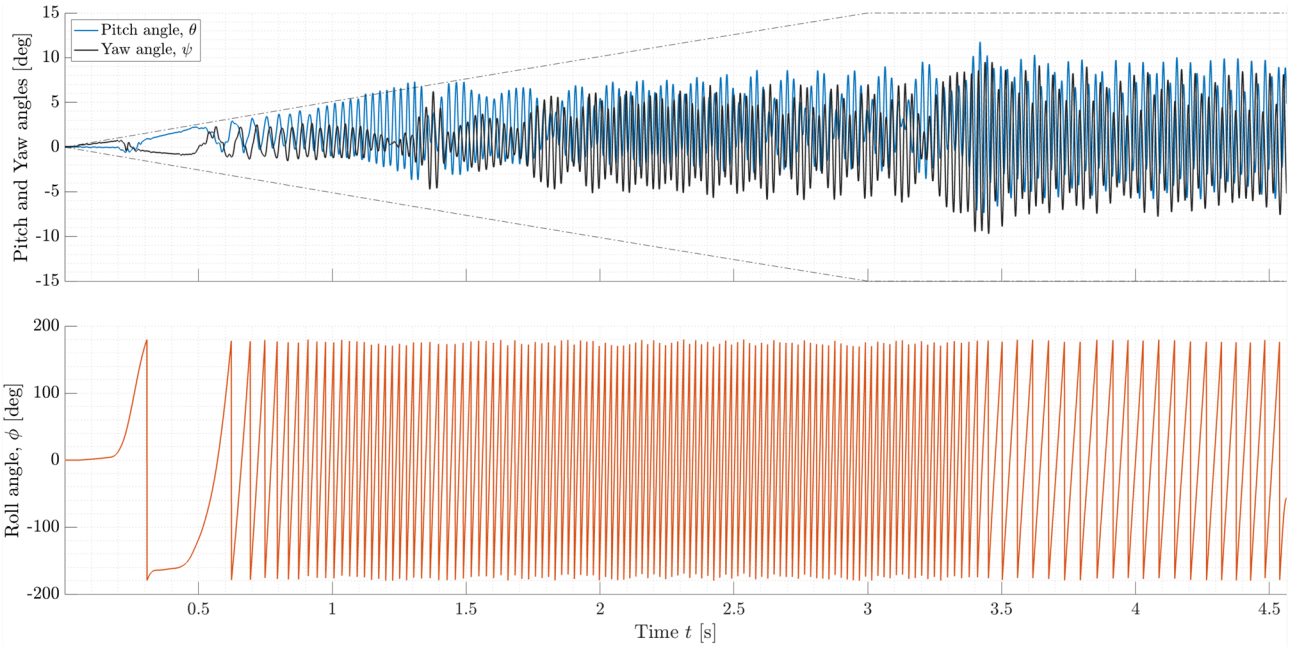

(a) Euler angles vs time

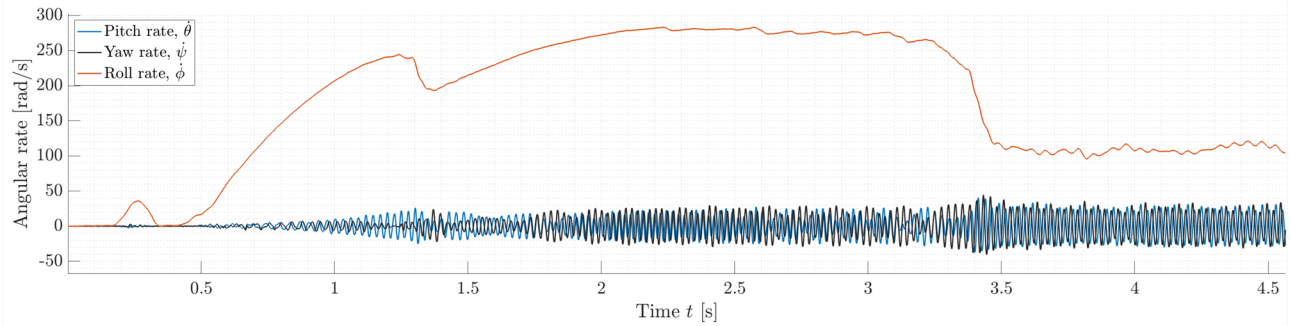

(b) Euler angular rates vs time

Fig. 15 Euler angles and rates for the faceted aeroshell model with roll generators at $M = 2$, measured with photogrammetry

frequencies were selected for roll and for pitch/yaw: $f_{c,\phi} = 30$ Hz for roll, and $f_{c,\theta} = f_{c,\psi} = 100$ Hz for pitch and yaw, respectively. Figure 15b highlights how the roll rate increases nonlinearly with time, as aerodynamic damping increases with roll rate. Also, as the limit cycle amplitude increases, the static roll moment induced by the roll generators decreases. This eventually leads to an equilibrium with a maximum roll rate of 283 rad/s. At $t = 3.4$ s, the model undergoes a sudden increase in pitch angle and a decrease in roll rate, which then stabilises at approximately 105 rad/s. The cause of this amplitude increase is discussed below. The different limit cycle amplitudes mentioned above correspond to the two distinct roll rate values.

3.2.3 Precessional instability

To gain insight into the physics driving the dynamics, the solution is fit to the tricyclic motion theory developed by Nicolaides (1953). The theory provides a closed-form solution to the simplified equations of free-flight motion of a rolling vehicle, achieving comparable accuracy to 6-DoF trajectory simulators. The total angle of attack is described in time as:

$$i\overline{\alpha} + \overline{\beta} = K_0 + K_n e^{(\lambda_n + i\omega_n)t} + K_p e^{(\lambda_p + i\omega_p)t} + K_t e^{i\dot{\phi}t} \tag{4}$$

where α and β are the angle of attack and of sideslip respectively, expressed in the aeroballistic frame of reference

(denoted by an overbar), $\lambda_{n,p}$ are the damping terms, and $\omega_{n,p}$ are the nutation and precession frequencies. The complex variables K_0, K_n, K_p and K_t depend on initial conditions, freestream conditions, vehicle properties, aerodynamic derivatives, and roll rate (see Vaughn (1968) for a derivation of Eq. 4). K_0 represents the non-rolling trim of the model. In this study, a nonzero K_0 is expected due to the CoG offset along the roll axis, as well as the strut connecting the rig to the wind tunnel ceiling, which causes a non-axisymmetric wake, and to a small angle ($< 0.6°$, non-uniform) of the incoming freestream flow. K_n and K_p represent the nutation and precession mode amplitudes. K_t represents the rolling trim amplitude, caused by a configurational asymmetry such as an aerodynamic trim, a CoG offset in the pitch/yaw plane, asymmetric boundary layer transition, and any other asymmetry that rolls with the model. In this work, a nonzero K_t is expected due to small mass non-uniformities introduced by the manufacturing process. The amplitude of K_t increases with $\dot{\phi}$ and has a singularity when $\dot{\phi} = \omega_n$, i.e. when the roll rate matches the nutation frequency. When this happens, the limit cycle amplitude increases abruptly and the vehicle undergoes roll resonance, which can lead to increased drag and offset trajectories at best and catastrophic failure at worst. The motion history in Fig. 15 reveals a maximum amplitude in total angle of attack for roll rates of about 100 rad/s and lower amplitudes for roll rates around 280 rad/s. Since K_t increases with roll rate, the increased oscillation amplitude at lower roll rates experienced at $t \geq 3.4$ s is expected to be unrelated to roll resonance and rather driven by the amplification of another mode.

Equation 4 is fit to the motion data shown in Fig. 15a, showing the measured angle of attack and sideslip in the aeroballistic coordinate frame alongside the fit. The residuals (shown in Fig. 16b) are lower than 1° for most of the run, indicating that the tricyclic equation closely captures the dynamics.

Figure 17 presents the tricyclic theory variables (frequencies and mode amplitudes) obtained with the nonlinear least square fit of the measured data. Figure 17a shows the nutation and precession frequencies obtained with the fit

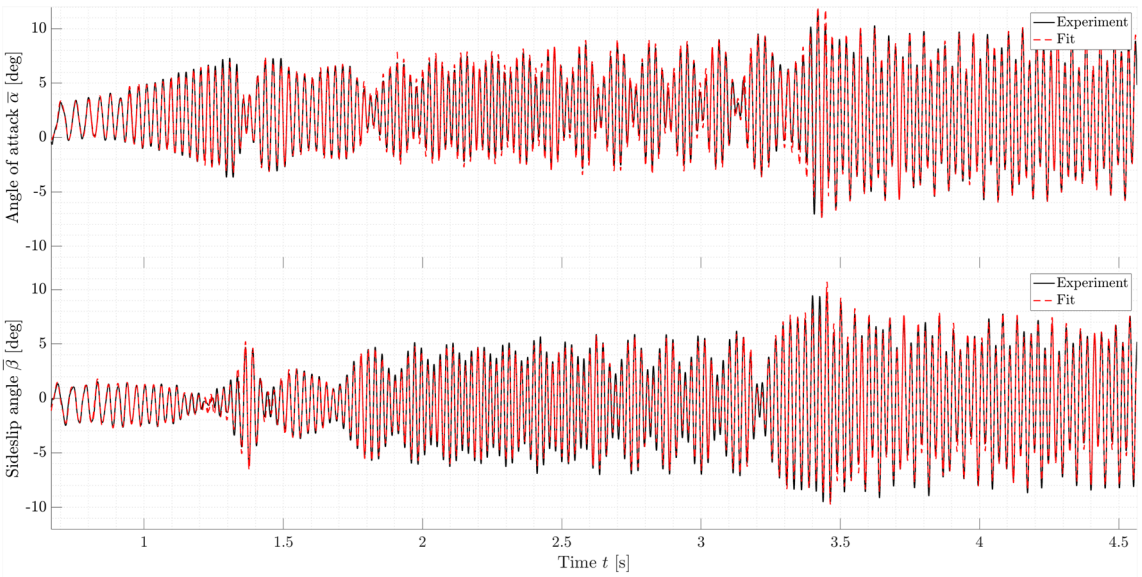

(a) Angle of attack and of sideslip in aeroballistic coordinate frame: experimental vs fit

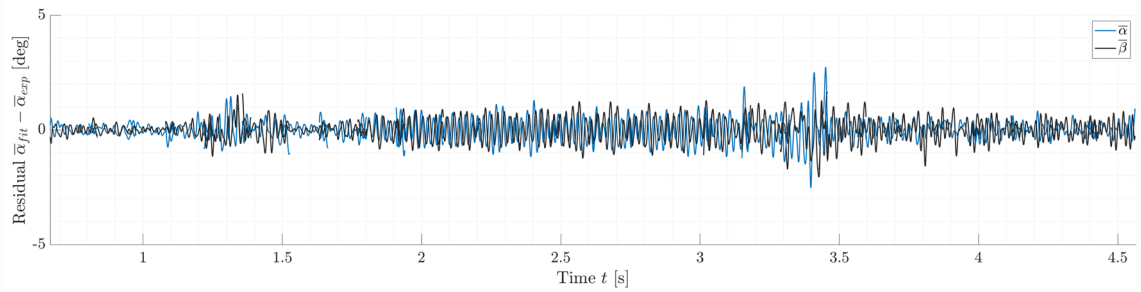

(b) Residuals

Fig. 16 Fit of the tricyclic theory (Eq. 4) with measured free-oscillation motion

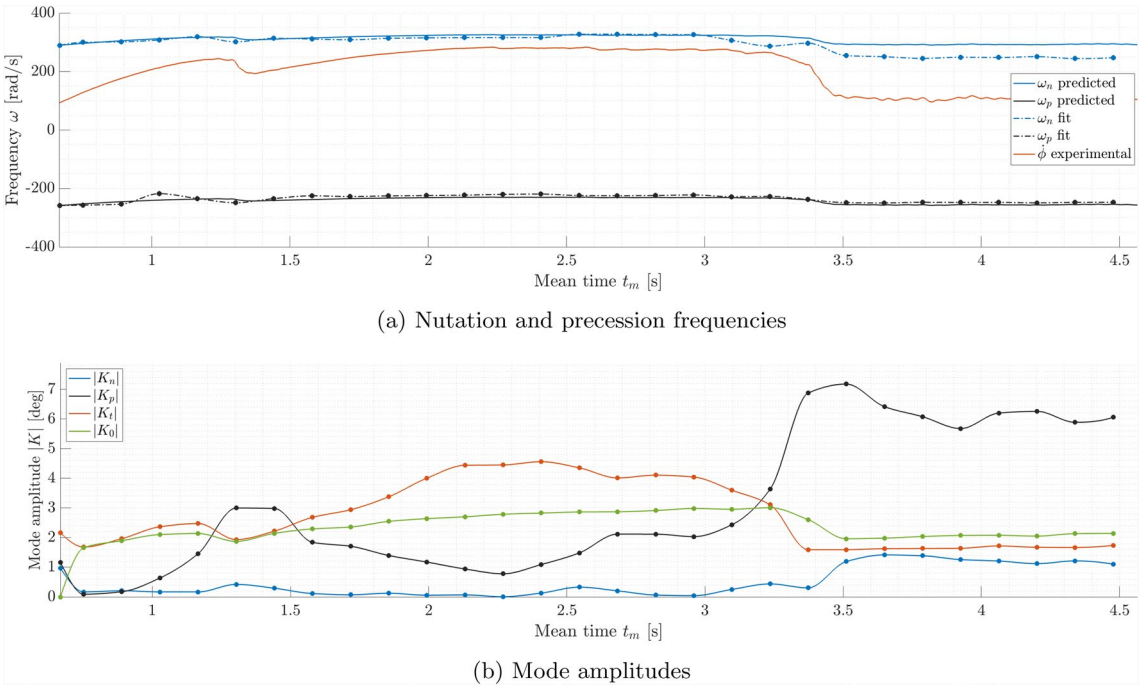

Fig. 17 Tricyclic motion variables obtained with nonlinear least square fit of motion data

alongside their undamped values (predicted by the tricyclic theory) and the experimental roll rate. The fit and predicted values agree closely except for deviations of the nutation frequency towards the end of the run. This is possibly due to the presence of aerodynamic damping (not accounted for in the predicted value), which decreases the oscillation frequency, as well as limitations of the theory (which assumes small angles and constant aerodynamic coefficients), unphysical behaviour of the model (due to interactions with the rig), and measurement errors. The roll rate $\dot{\phi}$ approaches the nutation frequency ω_n but never crosses it, indicating that the model does not lock into resonance. The increase in roll rate is reflected by the increase in amplitude of the rolling trim mode K_t, see Fig. 17b

Results are compared with tests performed by Ward et al. (1972) on a 9° semicone model ($L = 67.5$ cm) with

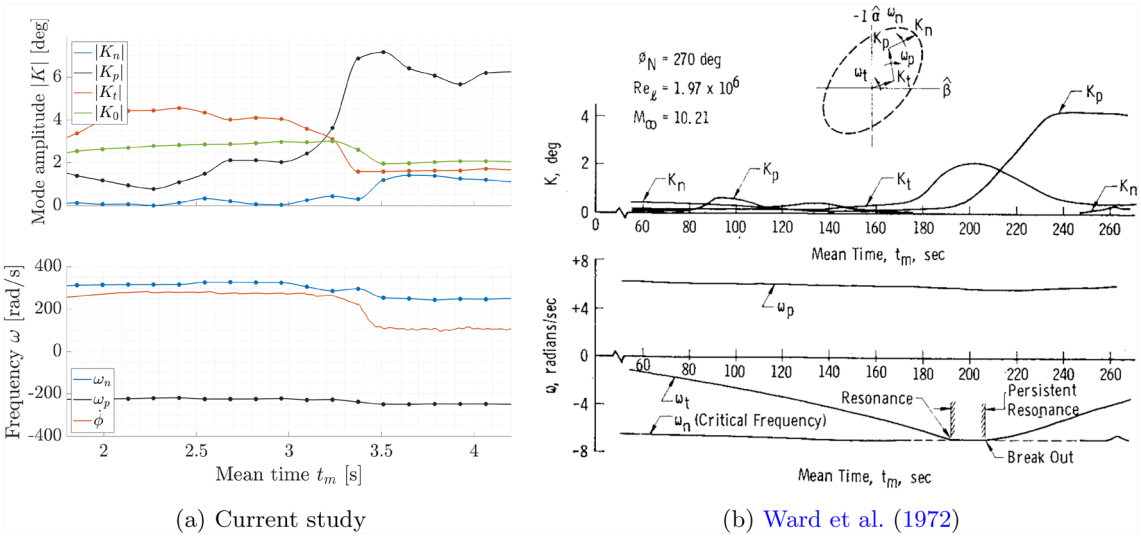

Fig. 18 Comparison with literature of tricyclic mode amplitudes and frequencies: **a** current study, blunt body at $M = 2$; **b** Ward et al. (1972), slender body at $M = 10.21$ ($\omega_t = \dot{\phi}$)

configurational asymmetries and canted fins at $M = 10.21$ (see Fig. 18). Note that the angular rates in the present study (Fig. 18a) are two orders of magnitude higher than those in Fig. 18b, suggesting a transition between two distinct rigid-body modes, each defined by a limit cycle amplitude and by an equilibrium between the static roll moment and the aerodynamic damping in roll. The first mode, observed from $t = 1.7$ s to $t = 3.2$ s and dominated by K_t, is characterised by high roll rates and limited oscillations in pitch and yaw. Once the limit cycle exceeds a critical amplitude ($t \simeq 3.4$ s), the effectiveness of the roll generators drops. In response to the abrupt decrease in static roll moment, the system jumps into a precession-dominated regime, characterised by a high-amplitude limit cycle and a low roll rate.

While roll generators of this kind are unlikely to be present in an actual deployable aeroshell, geometric asymmetries in roll can develop due to ablation during entry, as well as folding and warping of the flexible TPS that characterises some concepts (e.g. ADEPT, IRENE), thus leading to roll moments and potential instabilities of this kind. Notably, while precessional instabilities had previously been documented only by Ward et al. (1972) for slender bodies at high-hypersonic speeds, the present study demonstrates their occurrence for the first time in a blunt body at low supersonic speeds. This instability is particularly critical for spin-stabilised vehicles, due to the sudden decrease in roll rate combined with the large limit cycle amplitude.

4 Conclusion

A photogrammetry method has been implemented to a 3-DoF free-oscillation rig to measure hundreds of oscillations cycles during supersonic wind tunnel tests ($M = 2$). The model is a blunt body characterised by a faceted forebody and open aftbody, resembling the geometry of mechanically deployable aeroshells, with roll generators added to its panels. During supersonic runs, the estimated static and dynamic accuracy of the measurement is within 1°. The model dynamics are fit to the tricyclic motion theory and showcase the occurrence of a precessional instability which has been previously reported only for slender bodies in high-hypersonic regimes.

Acknowledgements The first author would like to acknowledge the Department of Mechanical Engineering at Imperial College London for funding the present research.

Author Contributions P.I. contributed to conceptualization, performed the wind tunnel experiments, post-processed the data, and wrote the first draft of the manuscript. P.B. and S.N.M. contributed to conceptualization, supervised the research, and reviewed the manuscript.

Data Availability No datasets were generated or analysed during the current study.

Declarations

Conflict of interest The authors declare no conflict of interest.

References

Brooks JD, Beamish JK (1977) Measurement of Model Aeroelastic Deformations in the Wind Tunnel at Transonic Speeds Using Stereophotogrammetry. Technical report, NASA Technical Paper 1010

Baqersad J, Poozesh P, Niezrecki C, Avitable P (2017) Photogrammetry and optical methods in structural dynamics–a review. Mech Syst Signal Process 86:17–34. https://doi.org/10.1016/j.ymssp.2016.02.011

Bassano E, Savino R, Forti RL, Ferrarotti A, Richiello C, Russo G, Aurigemma R, Punzo F, Dell'Aversana P (2011) IRENE: Italian re-entry Nacelle for microgravity experiments. In: Proceedings of the 62nd international astronautical congress (IAC), Cape Town, South Africa. https://doi.org/10.13140/2.1.3811.2642

Cassell A, Brivkalns C, Bowles J, Garcia J, Kinney D, Wercinski P, Cianciolo A, Polsgrove T (2017) Human mars mission design study utilizing the adaptive deployable entry placement technology. In: Proceedings of the IEEE aerospace conference. AIAA, Big Sky, Montana, USA. https://doi.org/10.1109/AERO.2017.7943585

Dutta S, Karlgaard C, Korzun A, Green J, Tynis J, Williams J, Yount B, Cassell A, Wercinski P (2022) Adaptable deployable entry and placement technology sounding rocket one modeling and reconstruction. J Spacecr Rocket 60(5):236–259. https://doi.org/10.2514/1.A35090

Gramola M, Bruce PJK, Santer MJ (2019) Photogrammetry for accurate model deformation measurement in a supersonic wind tunnel. Exp Fluids. https://doi.org/10.1007/s00348-018-2652-7

Gramola M, Bruce PJK, Santer MJ (2022) Hypersonic Foldable Aeroshell for THermal protection using ORigami (HATHOR): Aerothermal Analysis. In: AIAA SciTech 2022 Forum. AIAA, San Diego, CA and Virtual. https://doi.org/10.2514/6.2022-2288

Hergert JD, Brock JM, Stern EC, Wilder MC, Bogdanoff DW (2017) Free-flight trajectory simulation of the ADEPT sounding rocket test using CFD. In: AIAA 35th applied aerodynamics conference. AIAA, Denver, Colorado. https://doi.org/10.2514/6.2017-4462

Hyslop A, Doherty LJ, McGilvray M (2024) Comparison of force measurement techniques in a short-duration hypersonic facility. Exp Fluids 65:21. https://doi.org/10.1007/s00348-024-03761-9

Hartley R, Trumpf J, Dai Y, Li H (2013) Rotation averaging. Int J Comput Vis 103:267–305. https://doi.org/10.1007/s11263-012-0601-0

Hartley R, Zisserman A (2004) Algorithm Evaluation and Error Analysis. Multiple View Geometry in Computer Vision, 2nd edn. Cambridge University Press, Cambridge, pp 117–129

Innocenzi P, Bruce PJK, Navarro-Martinez S (2025) Mach, reynolds, and strouhal number effects on deployable aeroshell pitch dynamics. J Spacecr Rocket 62(5):1555–1566. https://doi.org/10.2514/1.A36126

Innocenzi P, Gramola M, Fisher TB, Quinn MK, Bruce PJK, Navarro-Martinez S (2022) Aerothermodynamic analysis of faceted aeroshell at hypersonic speed. In: HiSST: 2nd international conference on high-speed vehicle science technology, Bruges, Belgium. https://doi.org/10.48550/arXiv.2311.13487

Judd S (2023) Revisiting reentry roll resonance. J Spacecr Rocket 60(5):1448–1457. https://doi.org/10.2514/1.A35567

Kazemba CD, Braun RD, Clark IG, Schoenenberger M (2017) Survey of blunt-body supersonic dynamic stability. J Spacecr Rocket 54(1):80–96. https://doi.org/10.2514/1.A33552

Kushner LK, Littell J, Cassell A (2013) Photogrammetry of a Hypersonic Inflatable Aerodynamic Decelerator. In: AIAA aerodynamic decelerator systems (ADS) conference. AIAA, Daytona Beach, FL . https://doi.org/10.2514/6.2013-1284

Li L, Braun RD, Cassell A (2014) Photogrammetry analysis of a hypersonic inflatable aerodynamic decelerator structural test article. In: AIAA SciTech 2014 Forum. AIAA, National Harbor, MD . https://doi.org/10.2514/6.2014-0353

Lock A, Hack F, Jahn I, Armstrong G, Birch B, Buttsworth D (2025) Aerodynamic measurements of hypersonic free-flight via optical tracking and bayesian state estimation. AIAA J 63(5):1681–1697. https://doi.org/10.2514/1.J064061

Muller L, Libsig M, Martinez B, Bidino D, Bastide M, Bailly Y, Roy JC (2019) Numerical and experimental investigation of a three-axis free rotation wind tunnel model. In: 54th 3AF International conference on applied aerodynamics, Paris, France . https://doi.org/10.48550/arXiv.2305.08578

Muller L, Libsig M, Martinez B, Bidino D, Bastide M, Bailly Y, Roy JC (2020) Wind tunnel measurements of the dynamic stability derivatives of a fin-stabilized projectile by means of a three-axis freely-rotating test bench. In: AIAA Aviation 2020 Forum. AIAA, Virtual Event. https://doi.org/10.2514/6.2020-2782

Nicolaides J (1953) On the free flight motion of missiles having slight configurational asymmetries. Technical Report, Ballistic Research Laboratories, Report No. 858

Owens DB, Aubuchon VV (2011) Overview of Orion Crew Module and Launch Abort Vehicle Dynamic Stability. In: 29th AIAA applied aerodynamics conference, Honolulu, Hawaii . https://doi.org/10.2514/6.2011-3504 . AIAA. AIAA Paper 2011-3504

O'Driscoll DS, Bruce PJK, Santer M (2021) Design and dynamic analysis of rigid foldable aeroshells for atmospheric entry. J Spacecr Rocket 58(3):741–753. https://doi.org/10.2514/1.A34845

Owens B, Weinstein R, Giles I (2024) Aerodynamic Stability of the Dragonfly Aeroshell in the Transonic Dynamics Tunnel. American Institute of Aeronautics and Astronautics, Orlando, FL, USA. Invited presentation. https://ntrs.nasa.gov/citations/20230018629

PhotoModeler Technologies: PhotoModeler User Manual (2022)

Schairer ET, Hand LA (1999) Measurements of unsteady aeroelastic model deformation by stereo photogrammetry. J Aircr 36(6):1033–1040. https://doi.org/10.2514/2.2545

Sorkine-Hornung O, Rabinovich M (2017) Least-Squares Rigid Motion Using SVD. Technical Report, Department of Computer Science, ETH Zurich

Schairer ET, Heineck JT, Spooner H, Overmeyer AD (2021) Blade displacement measurements of a rotor in forward flight in the langley 14- by 22-foot wind tunnel. In: AIAA SciTech 2021 Forum. AIAA, Virtual Event . https://doi.org/10.2514/6.2021-0131

Schairer ET, Kushner LK, Drain BA, Heineck JT, Durston DA (2017) Stereo photogrammetry measurements of the position and attitude of a nozzle-plume/shock-wave interaction model in the NASA Ames 9- by 7- Ft supersonic wind tunnel. In: 55th AIAA aerospace sciences meeting. AIAA, Grapevine, TX. https://doi.org/10.2514/6.2017-1053

Starshak WC, Laurence SJ (2021) Computer-graphics-based optical tracking for hypersonic free-flight experiments. AIAA J 59(12):4752–4767. https://doi.org/10.2514/1.J060017

Seltner PM, Willems S, Gülhan A (2019) Aerodynamic coefficients of free-flying cubes in hypersonic Flowfield. J Spacecr Rocket 56(6):1524–1535. https://doi.org/10.2514/1.A34345

Schueler CJ, Ward LK, Hodapp Jr AE (1967) Techniques for Measurement of Dynamic Stability Derivatives in Ground Test Facilities. AGARDograph No. 121. Advisory Group for Aerospace Research and Development (AGARD), NATO, Paris, France

Threadgill JAS (2017) Unsteadiness of Shock Wave Boundary Layer Interactions Across Multiple Interaction Configurations and Strengths. PhD thesis, Imperial College London. https://doi.org/10.25560/48475

Vaughn H (1968) A Detailed Development of the Tricyclic Theory. Technical report, Sandia National Laboratory, Report SC-M-67-2933

Watzlavick RL, Crowder JP, Wright FL (1996) Comparison of model attitude systems: active target photogrammetry, precision accelerometer, and laser interferometer. In: 19th Advanced measurement and ground testing technology conference. AIAA, New Orleans, LA. https://doi.org/10.2514/6.1996-2252

Whitlock CH, Siemers PM (1972) Parameters influencing dynamic stability characteristics of viking-type entry configurations at Mach 1.76. J Spacecr Rocket 9(7):558–560. https://doi.org/10.2514/3.61741

Ward KL Jr, Uselton JC, Billingsley JP (1972) Three-degree-of-freedom motions of a slender asymmetric cone in a hypersonic wind tunnel. J Spacecr Rocket 9(11):831–835. https://doi.org/10.2514/3.30401